Synthesis, Structure, Photoluminescence, and Optical Properties of (Co/B) Co-Doped ZnO Nanoparticles

L. Arda,* S. Veziroglu, K. Ozdogan, and E. Ozugurlu

Co/B co-doped ZnO nanoparticles, denoted as $Zn_{0.95-x}B_xCo_{0.05}O$, are synthesized using the sol–gel method to explore the effects of the defects on optical properties. The stoichiometry is adjusted by varying the doping levels (x = 0.00, 0.01, 0.02, 0.03, 0.04, and 0.05). X-ray diffraction is employed to analyze the structural characteristics of all Co/B co-doped ZnO nanoparticles, confirming the presence of a hexagonal Wurtzite structure by assessing the c/a ratios. To investigate structural defects, photoluminescence properties are measured using the Fluorescence Spectrophotometer, revealing violet, blue, green, and red emissions. With the doped of boron (B), a shift from green emission to blue emission occurs, indicating a transformation of singly charged oxygen vacancies (V_O^+) to V_{Zn} vacancies. Fourier Transform Infrared (FTIR) spectra (4000–400 cm^{-1}) are acquired using the Perkin Elmer Spectrum Two FTIR-ATR spectrophotometer. The surface morphology, crystallite size, and nanoparticle shapes are characterized through Transmission Electron Microscope (TEM) analysis. Elemental compositions are determined using Electron Dispersive Spectroscopy (EDAX). The Shimadzu 2600 UV-Spectrophotometer is used to examine optical characteristics. The samples' energy band gaps are calculated, and the impact of dopant elements on these optical characteristics is examined. Five different models are used to compute the refractive index.

L. Arda
Department of Mechatronic Engineering
Bahcesehir University
Besiktas, Istanbul 34353, Türkiye
E-mail: lutfi.arda@bau.edu.tr

S. Veziroglu
Graduate School of Science and Engineering
Yildiz Technical University
Esenler, Istanbul 34220, Türkiye

S. Veziroglu
Department of Physics
Faculty of Science
Marmara University
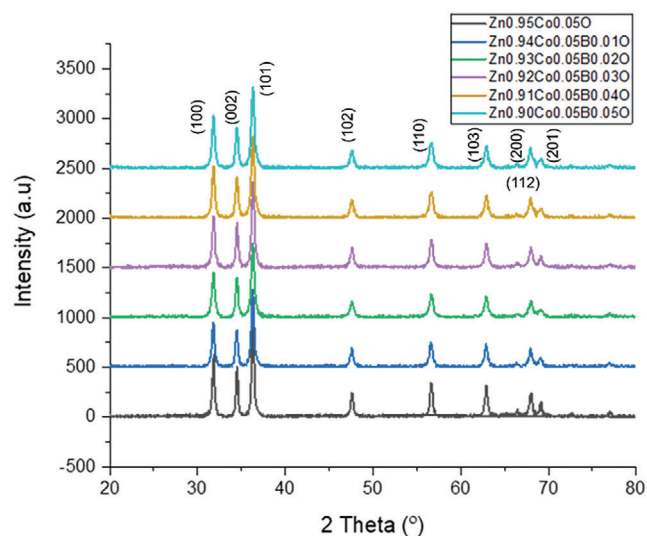Kadikoy, Istanbul 34722, Türkiye

K. Ozdogan
Department of Physics
Yildiz Technical University
Esenler, Istanbul 34220, Türkiye

E. Ozugurlu
Department of Mathematics
Istanbul Technical University
Maslak, Istanbul 34469, Türkiye

The ORCID identification number(s) for the author(s) of this article can be found under https://doi.org/10.1002/ppsc.202400140

1. Introduction

Because of its exceptional performance in the domains of optics, photonics, and electronics as well as its distinct physical and chemical properties, nanostructured ZnO has drawn a lot of interest and has been used in many areas,[1–6] especially in detectors technologies that use solid-state light sources and the blue and UV spectral bands due to its wide band gap (3.37 eV) at ambient temperature[7] and is a preferred material in the transparent contacts of solar cells because of its high radiation characteristics as well as its resilience to heat and chemicals. ZnO doping using transition metals (TMs) has been the subject of numerous investigations. Among the applications is spintronic, which is a field of electronics in which the electron spin is manipulated to obtain the desired result, and in which the energy band gap and electrical conductivity play a very large role, thus it is crucial to decide which ZnO elements need to be doped to raise the carrier concentration.[8]

High refractive index (n) and wide band gap (E_g) materials have garnered significant attention due to their utility in the fields of optoelectronics and sensor technology. These properties are instrumental in enhancing the performance of optical interference filters and optical sensors, particularly in applications such as anti-reflection coatings. Naccarato et al.[9] showed in 2019 how the chemistry affected the relationship between the high refraction index and band gap and why some material classes out of 4000 semiconductors would perform better. They looked over a few of the band gap-based refractive index computation models. The models in question are those developed by, Ravindra et al.,[10] Moss,[11] Hervé and Vandamme,[12] Redd and Anjaneyulu,[13] and Kumar and Singh.[14] Zinc oxide (ZnO) is an excellent choice for functional components of devices and materials; in photonic crystals, spintronic, microelectronics, solar cells, lasers, varistors, photoelectrochemical cells, gas sensors, light-emitting diodes.[15–23] Selecting the element or elements that need to be doped into ZnO to regulate the band gap, enhance carrier concentration, and increase electrical conductivity is critical. Because of the possible applications, doping ZnO with transition metals (TMs) and rare earth elements including Cu, Co, Er, Cr, Yb, Fe, Mg, Ni, Mn, Y, and Tb has been the subject of numerous publications published in the previous few decades.[24–36]

**ADVANCED
SCIENCE NEWS**
www.advancedsciencenews.com

Particle
& Particle Systems Characterization
www.particle-journal.com

Figure 1. XRD patterns of $Zn_{0.95-x}B_xCo_{0.05}O$ NPs at different B concentrations.

When Co atoms are added to zinc oxide, the lattice constant remains unchanged because their ionic radius (0.65 Å) is similar to those of Zn atoms (0.74 Å). Therefore, a great deal of research has been done on how Co doping affects the optoelectronic characteristics and magnetism of ZnO films that are made using spray pyrolysis, hydrothermal technique, sol–gel, pulsed laser deposition methods, magnetron DC sputtering, and magnetron RF sputtering.[20–27] According to several studies, adding Co to ZnO raises the ferromagnetic moment.[37] Boron has been used as a dopant recently because it is a cheap, readily available, non-toxic, and good conductor.[38] Additionally, because of Boron's small ionic radius (0.23 Å), it can function in the ZnO lattice as an interstitial one or a substituted one.[3,39] On the other hand, over-doping may deteriorate the crystal's quality. Therefore, determining the appropriate amount of doping is crucial.

In this study, first time $Zn_{0.95-x}B_xCo_{0.05}O$ nanoparticles (NPs) were synthesized using the sol–gel method by varying the dopant ratio from x = 0.00 to 0.05 with an increment of 0.01. We performed photoluminescence studies to determine the key variables affecting structural and optical performance. Notably, we detected the formation of Zn vacancies (V_{Zn}), oxygen vacancies (V_o), interstitial Zn (Zn_i), and singly charged oxygen vacancies (V_o^+), With the boron doping, the green emission shifted to blue emission, indicating a transformation of singly charged oxygen vacancies (V_o^+) into V_{Zn} vacancies, suggesting the presence of acceptors instead of donors. This research contributes valuable insights into the defect phenomenon, which has been underreported in the existing literature.

2. Results and Discussion

2.1. Structural Characterization

X-ray Diffraction (XRD) analysis was employed to investigate the structural characteristics of $Zn_{0.95-x}B_xCo_{0.05}O$ NPs within the angular range of $20° \leq 2\theta \leq 80°$, with peak positions accu-

Table 1. $Zn_{0.95-x}B_xCo_{0.05}O$ (x = 0.00−0.05) NPs concentration dependent average crystallite sizes (D), lattice characteristics, atomic packing factor (c/a), crystal lattice distortion degree, and volume of the unit cell.

Sample name	D [nm]	a [Å]	c [Å]	c/a	Volume V [Å³]
$Zn_{0.95}Co_{0.05}O$	27.251	3.2389	5.1924	1.6031	47.173
$Zn_{0.94}B_{0.01}Co_{0.05}O$	24.132	3.2447	5.1952	1.6011	47.367
$Zn_{0.93}B_{0.02}Co_{0.05}O$	24.290	3.2467	5.1924	1.5993	47.398
$Zn_{0.92}B_{0.03}Co_{0.05}O$	22.652	3.2447	5.1982	1.6021	47.394
$Zn_{0.91}B_{0.04}Co_{0.05}O$	21.903	3.2447	5.1954	1.6012	47.368
$Zn_{0.90}B_{0.05}Co_{0.05}O$	21.890	3.2436	5.1952	1.6017	47.333

rately indexed. As depicted in **Figure 1**, the XRD patterns revealed the presence of the ZnO phase with a wurtzite hexagonal structure (ICDD card No. 36–1451) belonging to space group P63mc.

By performing XRD analysis on both $Zn_{0.95}Co_{0.05}O$ and $Zn_{0.95-x}B_xCo_{0.05}O$ (x = 0.01, 0.02, 0.03, 0.04, 0.05) NPs, we were able to calculate and document several concentration-dependent parameters. These included the lattice parameters, average crystallite sizes, volume of the unit cell, stress (σ), microstrain (ϵ), dislocation density (δ) (a measure of defect concentration in the sample), the local arrangement of atoms, their displacement (u), and bond length (L), all of which are listed in **Tables 1** and **2**. For a comprehensive understanding of the calculations of ϵ, σ, δ, D, u, and L parameters, detailed information can be found in reference.[25,26]

The ZnO bond length is determined by applying the following Equation (1):[3,25]

$$L = \sqrt{\left(\frac{a^2}{3}\right) + [0.5 - u]^2 c^2} \qquad (1)$$
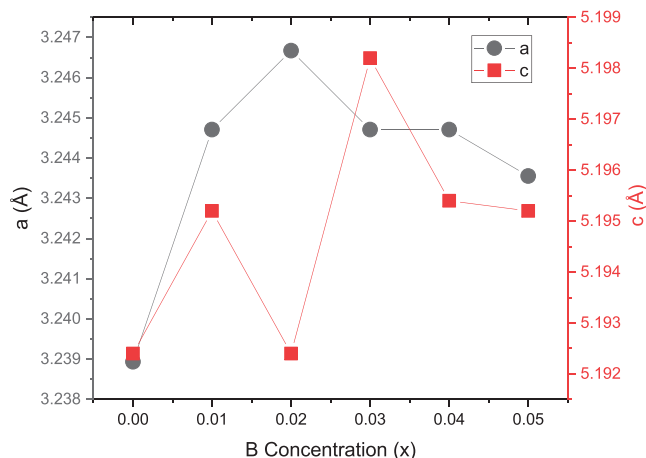
in which u is the atomic position parameter for wurtzite structure, which may be computed using Equation (2);

$$u = \left(\frac{a^2}{3c^2}\right) + 0.25 \qquad (2)$$

Here, a and c are the lattice constant of ZnO.

Table 2. The varying concentration-dependent microstrain ($\mathcal{E}$), stress (σ), dislocation density (δ) (the amount of defect in the sample), the locality of the atoms and their displacement (u), and bond length (L) in $Zn_{0.95-x}B_xCo_{0.05}O$ (x = 0.00−0.05) NPs.

Sample name	$\mathcal{E}$	$\sigma \times 10^9$ [N m⁻²]	δ [nm⁻²]	u	L [Å]
$Zn_{0.95}Co_{0.05}O$	0.00127	−22.8865	0.00135	0.3797	1.9716
$Zn_{0.94}B_{0.01}Co_{0.05}O$	0.00144	−22.8735	0.00172	0.3800	1.9743
$Zn_{0.93}B_{0.02}Co_{0.05}O$	0.00143	−22.6360	0.00169	0.3803	1.9748
$Zn_{0.92}B_{0.03}Co_{0.05}O$	0.00153	−23.1679	0.00195	0.3799	1.9747
$Zn_{0.91}B_{0.04}Co_{0.05}O$	0.00158	−23.1618	0.00208	0.3800	1.9743
$Zn_{0.90}B_{0.05}Co_{0.05}O$	0.00158	−23.1434	0.00209	0.3799	1.9738

**ADVANCED
SCIENCE NEWS**

www.advancedsciencenews.com

Particle
& Particle Systems Characterization

www.particle-journal.com

Figure 2. Lattice parameters (*a* and *c*) in $Zn_{0.95-x}B_xCo_{0.05}O$ structures that are concentration dependent.

For <100> and <002> planes, the lattice constants a and c are calculated in Equation (3):[3,25]

$$\frac{1}{d_{hkl}^2} = \frac{4}{3}\left(\frac{h^2 + hk + k^2}{a^2}\right) + \frac{l^2}{c^2} \quad (3)$$

Using the Debye-Scherrer Equation (4), the average crystallite size (*D*) was determined from the XRD spectra average of (100), (002), and (101) peaks.[3,25]

$$D = \frac{K\lambda}{\beta_{hkl}\cos(\theta)} \quad (4)$$

where λ is the incident X-ray wavelength ($\lambda = 0.1540$ nm), D is the crystallite size, θ is the Bragg angle, and β_{hkl} is the integral half-width. K is a constant set at 0.90.

Regarding ZnO NPs co-doped with B/Co, the lattice parameter *c*, as determined by analyzing the samples' (002) peaks, falls between 5.1924 Å and 5.1982 Å as shown in **Figure 2**. The lattice parameter ratio, c/a, appears to be fluctuating as shown in **Figure 3**. The optimal wurtzite structure has c/a = $\sqrt{(8/3)}$, or around 1.633. This ideal wurtzite structure is larger than the experimental values found in our investigation. Since B and Co ions have smaller ionic radii (0.23 Å and 0.65 Å, respectively) than Zn ionic radius (0.74 Å), such variations are true to be expected if B and Co ions replace Zn ions in the lattice.[40] In $Zn_{0.95-x}B_xCo_{0.05}O$ samples, the location of the atoms and their displacements (*u* parameters) were computed and showed nearly consistent behavior around 0.38. The optimal value for the ZnO wurtzite structure is u = 3/8 (0.375). The u values that were calculated are higher than 0.375. There was some fluctuation in the Zn-O bond lengths (L parameters) between 1.9716 and 1.9748 Å as shown in Figure 3 and 4.

The doping element and its ratio, synthesis techniques, and annealing temperature are a few examples of factors that might impact stress and strain in a structure. Therefore, stresses and strains may be the source of the physical defects and dislocations in NPs. We calculated microstrain and stress values of $Zn_{0.95-x}B_xCo_{0.05}O$ (x = 0.01, 0.02, 0.03, 0.04, 0.05) NPs and depicted in Table 2 and **Figure 5**. Without boron concentration, the
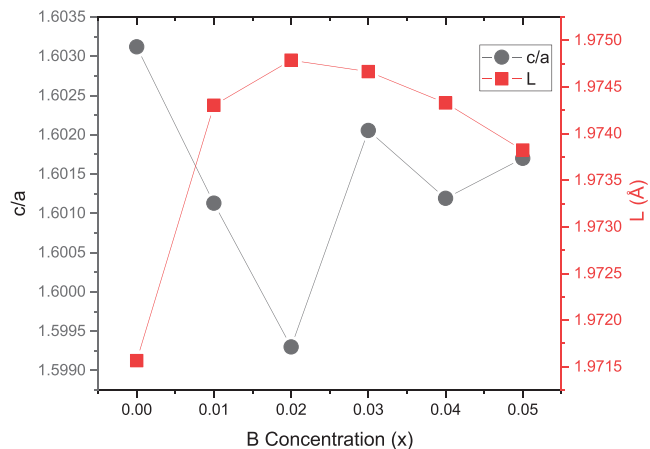
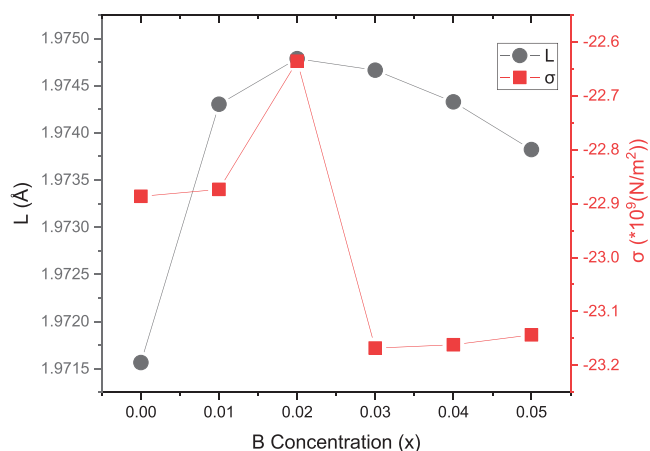**Figure 3.** Lattice parameters (*c/a*) and Zn-O bond lengths (*L*) in $Zn_{0.95-x}B_xCo_{0.05}O$ structures (x = 0.00, 0.01, 0.02, 0.03, 0.04, 0.05) that are concentration dependent.
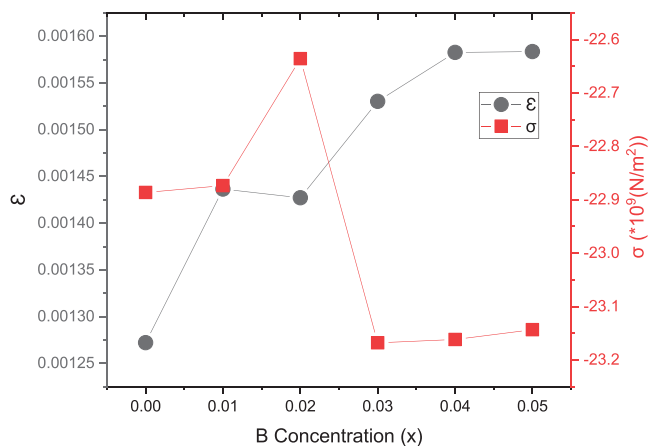
microstrain reached a minimum value of 0.00127, for the boron-doped ones microstrain ϵ started to increase except at x = 0.02 as shown in Table 2 which illustrates the negative signs of the σ values which show compressive stresses. These values show a reduction up until the dopant rate of x = 0.02, beyond which they fluctuate until a minimum value of −22.636 is attained. Numerous physical defects and dislocations in the host lattice structure may be seen by the variations in the strain and stress measurements. Thus, dislocation density (δ), which indicates the quantity of defects in the sample, was also examined. The crystallite diameters (D) of the crystallite samples decrease in response to the rise of B elements in the stoichiometric samples, as Table 2 and **Figure 6** illustrate.

At x = 0.00 (without boron), the highest crystallite size of 27.25 nm was reached. Because of the inverse proportion expression between δ and D values, dislocation density (δ) has shown a minimum value of 1.35×10^{-3} at x = 0.00.

The doping of ZnCoO NPs with Boron (B) was observed to decrease the crystallite size except for the 2% B doping ratio. This

Figure 4. Zn—O bond lengths (*L*) and stress (σ) values in $Zn_{0.95-x}B_xCo_{0.05}O$ structures (x = 0.00, 0.01, 0.02, 0.03, 0.04, and 0.05) are concentration-dependent.

ADVANCED
SCIENCE NEWS

www.advancedsciencenews.com

Particle
& Particle Systems Characterization

www.particle-journal.com
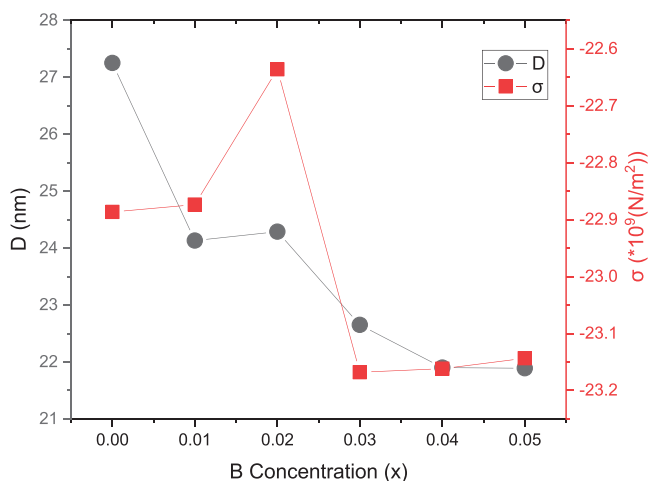
Figure 5. Microstrain (ϵ) and stress (σ) values in $Zn_{0.95-x}B_xCo_{0.05}O$ structures ($x = 0.00$, 0.01, 0.02, 0.03, 0.04, and 0.05) are concentration-dependent.

is an expected outcome because the ionic radius of B is smaller compared to Zn and Co. The single position parameter u reaches a maximum of 0.3803 at a 2% B concentration ratio, which is greater than the optimal value of $3/8 = 0.375$. The average crystallite size (D) decreases as the doping ratio increases, while microstrain ($\mathcal{E}$) and dislocation density (δ) increase, except for the 2% B doping ratio.

2.2. FTIR Studies

The FTIR spectrum of $Zn_{0.95-x}B_xCo_{0.05}O$ NPs is depicted in **Figure 7**. Notably, the primary transmittance bands fall within the range of 4000 to 400 cm^{-1}. The key peaks observed are as follows: O—H stretching or M—OH—M band in the range of 4000–3500 cm^{-1}.

C—H vibration spanning from 3200 to 1900 cm^{-1}. This region typically encompasses absorption bands related to the stretching vibrations of carbon—hydrogen (C—H) bonds in aliphatic hydro-

Figure 6. Average crystallite size (D) and stress (σ) values in $Zn_{0.95-x}B_xCo_{0.05}O$ structures ($x = 0.00$, 0.01, 0.02, 0.03, 0.04, and 0.05) are concentration-dependent.

carbons, which are organic compounds featuring open chains of carbon atoms, such as alkanes, alkenes, and alkynes.[41,42]

The C—C stretching occurs between 1750 and 1400 cm^{-1}, while the M—O band is observed below 1000 cm^{-1}. The bands associated with C—C stretching and bending exhibit a shift to lower frequencies with B doping, indicating a modification in the Zn—O bond due to B doping.

Peaks within the range of 400–480 cm^{-1} correspond to Zn—O bond stretching as shown in Figure 7b, whereas the band observed at 700 cm^{-1} could be attributed to B—O bond stretching. The absorption band was observed in un-doped $Zn_{0.99}Co_{0.01}O$ samples at 400 cm^{-1}. A rise in B doping from 1 to 5% resulted in a shift of the Zn—O stretching absorption band to 480 cm^{-1}. The absorption band's location was slightly shifted by the increase in boron content, which may have been caused by the B dopant ions being incorporated into the Zn—O lattice structure.[38] The stretching modes of ZnO were identified as the source of the distinctive absorption band at 400 cm^{-1}. Moreover, bond length was lowered by doping with smaller ionic radii, such as B^{2+} (0.23 Å) and Co^{2+} (0.65 Å), as opposed to Zn^{2+} (0.74 Å), which has a higher ionic radius. Therefore, the reduction in bond length in the FTIR spectrum in Figure 7 increased wavenumber. This may indicate stronger bonds or a greater energy requirement. The FTIR spectra, particularly within the range of 1100–400 cm^{-1}, present a notably complex pattern and offer comprehensive insights into the ZnO host material. It is feasible to deconvolute all spectra in this region. The stretching modes of ZnO-B-Co were identified within the range of 1250–750 cm^{-1}. This indicates the presence of defects in the system due to the incorporation of B and Co into the ZnO lattice. The defects were observed in PL measurements; see the PL section of the study for more details.

2.3. The Morphology Characteristics of NPs

The TEM picture of the Co/B co-doped ZnO NPs with varying sizes ranging from 20–200 nm is displayed in **Figure 8a–c**. The majority of the NPs appear to be clumped together in the TEM image. Based on the TEM data, it can be observed that the sol–gel NPs exhibit crystalline characteristics (Figure 8). The sharp XRD lines in Figure 1 are consistent with this outcome. Additionally, as seen in Figure 8, the crystalline nature of the NPs causes the atomic planes to appear to be aligned along the micrograph. The distance between planes is roughly 300.2 pm. All of the $Zn_{0.94}B_{0.01}Co_{0.05}O$ is shown in **Figure 9**. NPs' elemental composition was determined using the EDAX analysis shown in Figure 8d. In the EDAX analysis, every peak is part of the desired composition and does not contain any unwanted contributions from additional elemental peaks.

2.4. Photoluminescence (PL) Studies

Photoluminescence spectra are utilized for observing the crystal features, deficiency types, and imperfection densities of materials. Hence, we investigated the influence of Co/B concentration on the photoluminescence characteristics of ZnO NPs using PL. We acquired PL measurements of Co/B co-doped ZnO NPs with a 300 nm excitation wavelength, and the emitted lines were captured within the wavelength range of 350–850 nm, as illustrated
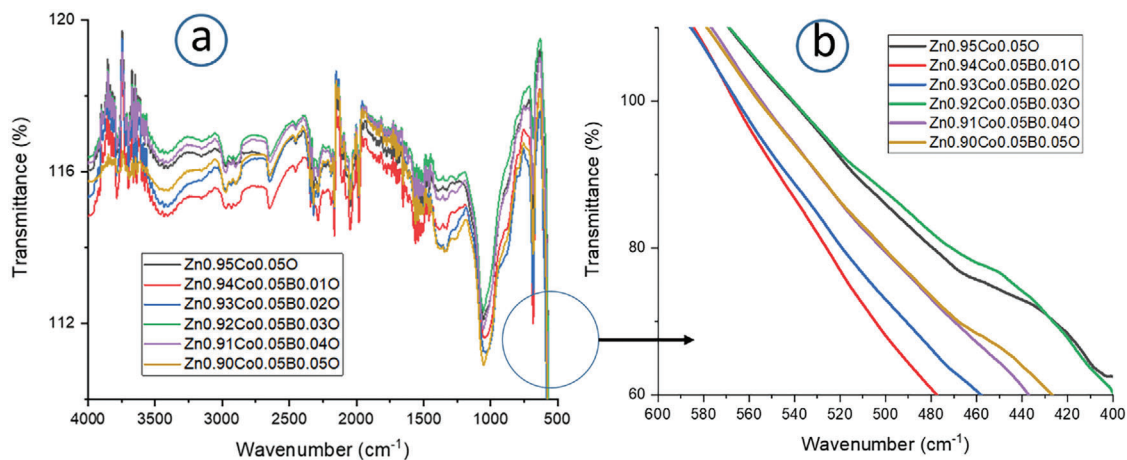
Figure 7. FTIR spectra of $Zn_{0.95-x}B_xCo_{0.05}O$ at different B concentrations.
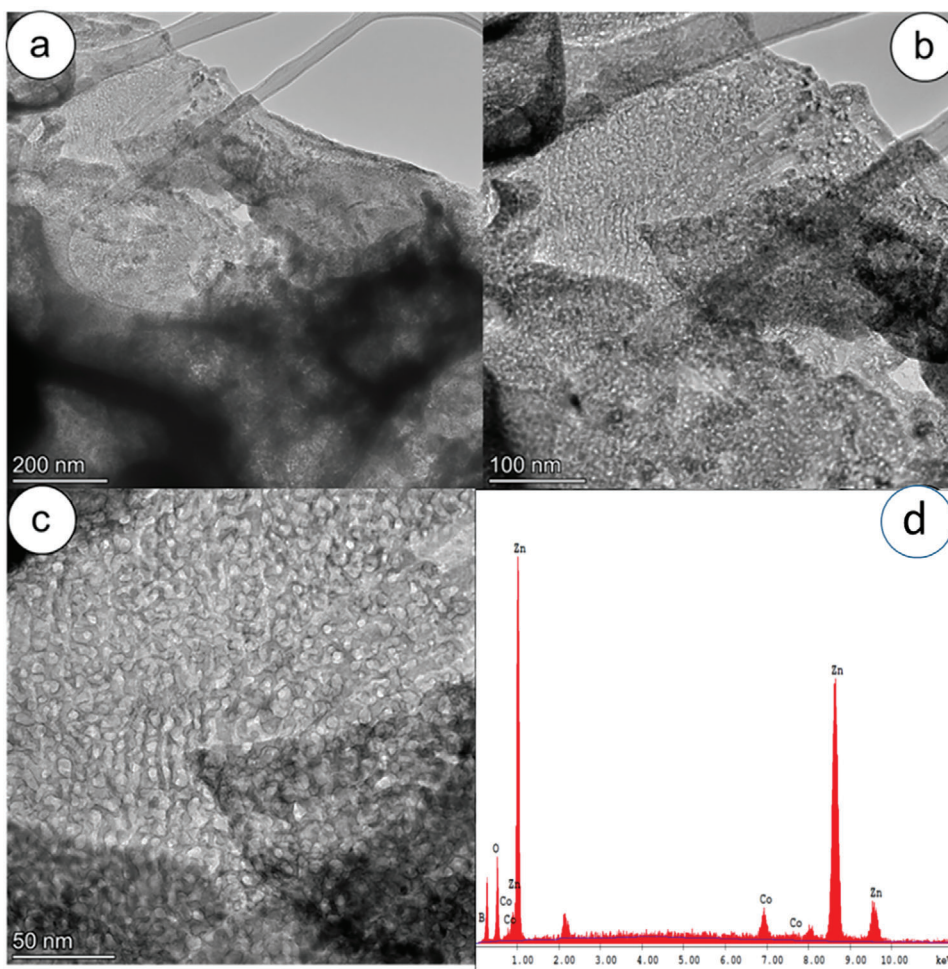
Figure 8. a–c) TEM images of $Zn_{0.94}B_{0.01}Co_{0.05}O$ NPs under different magnifications, and d) EDAX spectra of $Zn_{0.94}B_{0.01}Co_{0.05}O$ NPs.
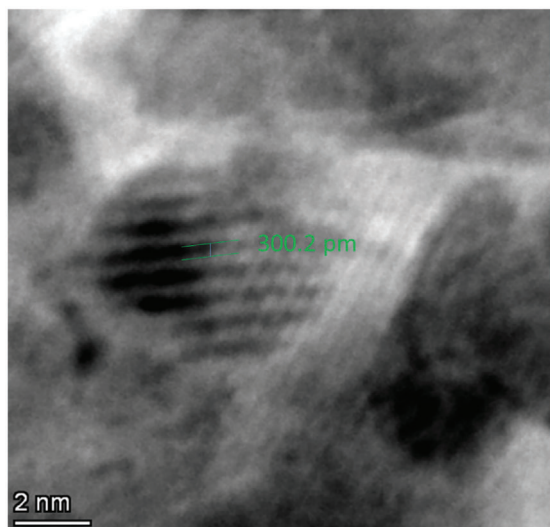
2400140 (5 of 12)

**ADVANCED
SCIENCE NEWS**

www.advancedsciencenews.com

Particle
& Particle Systems Characterization

www.particle-journal.com

Figure 9. TEM image of $Zn_{0.94}B_{0.01}Co_{0.05}O$ NPs (crystallographic planes are indicated between the two planes).

in **Figure 10**. The photoluminescence intensity of all NPs reached its peak at around 378–380 nm, as depicted in Figure 10. As the concentration of Boron varies, noticeable shifts in the peaks and changes in their intensities are observed. Two prominent emission peaks, representing the typical n-type ZnO semiconductor, are evident: a sharp ultraviolet emission peak and a broad visible emission band, as shown in Figure 10 (on the right column). It is established that ultraviolet emission reflects the crystallization quality and the number of defects in ZnO, whereas visible region emission is attributed to defects.[43,44]

One prominent optical property of ZnO's broad bandgap is the near band edge (NBE) transition, which is often linked with the ultraviolet region. Excitonic transitions between electrons in the conduction band and holes in the valence band are the source of NBE emission.[44] Greater UV emission in ZnO suggests better crystallization quality and fewer defects. Notably, NBE emission remains unchanged with variations in B concentration; only peak shifts are observed. Additionally, annealing at 600 °C yields a highly crystalline structure, a favorable outcome.

The second predominant wide emission spectrum encompasses the visible range, incorporating peaks spanning from violet to blue, green, yellow, orange, and red. This visible emission, referred to as deep-level (DL) emission, is attributed to impurities or defects such as oxygen vacancies (V_o), zinc vacancies (V_{Zn}), interstitial oxygen (O_i), interstitial zinc (Zn_i), and substitution of oxygen at a zinc position (O_{Zn}). These defects are divided into two groups: interstitial zinc vacancies (V_{Zn}), interstitial oxygen (O_i), and oxygen antisites (O_{Zn}), which function as acceptors, and interstitial zinc (Zn_i) and oxygen vacancies (V_o), which function as donors.[43–45] Through Gaussian decomposition, we discerned violet, blue, green, red, and NIR emission peaks, allowing for a detailed understanding of defect origins.

The photoluminescence spectra were subjected to Gaussian decomposition, revealing four main peaks corresponding to emission wavelength for varying Boron concentrations, as depicted in **Figure 11**. **Table 3** illustrates the peak labels, center positions, and heights for different B concentrations of ZnCoBO

NPs. These peaks comprise Peak 1 ultraviolet emissions, Peak 2: violet emissions and Peak 3 has two emission groups: blue emissions for B (1–5%) doping and green emissions for $Zn_{0.95}Co_{0.05}O$ (without B doping). Also, Peak 4 has two emission groups: red emissions for $Zn_{0.95}Co_{0.05}O$ and Near-Infrared peaks for B (1–5%), as detailed in Table 3. The emission regions outlined in Table 3 can be elucidated as follows: Ultraviolet emissions spanning from 379 to 380 nm are attributed to the near band edge (NBE) of $Zn_{0.95-x}B_xCo_{0.05}O$ structures (x = 0.00, 0.01, 0.02, 0.03, 0.04, and 0.05), signifying its excitonic nature.

Violet emissions in the range of 422–441 nm arise from electron transitions to the valence band from zinc interstitials (Zn_i) with varying charges, including neutral-Zn_i, single-Zn_i', and double-Zn_i'', as per the theoretical study by Singh and Gopal.[46] Blue emissions (475–480 nm) may be attributed to zinc vacancies (V_{Zn}), green emissions (541 nm) could be due to the single charged oxygen vacancy (Vo^+), and red emission (745 nm) could be ascribed to oxygen vacancies (V_O).

The Near-Infrared (NIR) region (>750 nm) is linked to secondary UV diffraction. Peak 4, for B (1–5%) doping ZnCoO NPs representing NIR emission, observed by Senol et al.,[45] could be caused by oxygen vacancies (V_O).

In conclusion, during the synthesis of $Zn_{0.95-x}B_xCo_{0.05}O$ NPs via sol–gel techniques, reactions result in the formation of Zn vacancies (V_{Zn}), oxygen vacancies (V_o), interstitial Zn (Zn_i), and singly charged oxygen vacancies (V_o^+), as shown in Table 3. Upon detailed examination of the peak heights provided in Table 3 and Figure 11, it is observed that oxygen vacancies (V_o), interstitial Zn (Zn_i), and singly charged oxygen vacancy (V_o^+) defects dominate, and $Zn_{0.95}Co_{0.05}O$ NPs exhibit donor defects that donate electrons to the conduction band. With the doped of boron (B), a shift from green emission to blue emission occurs, indicating a transformation of singly charged oxygen vacancies (V_o^+) to V_{Zn} vacancies. Additionally, it was observed that the peak heights of the violet emission decrease with boron doping, suggesting the presence of acceptor defects instead of donors.
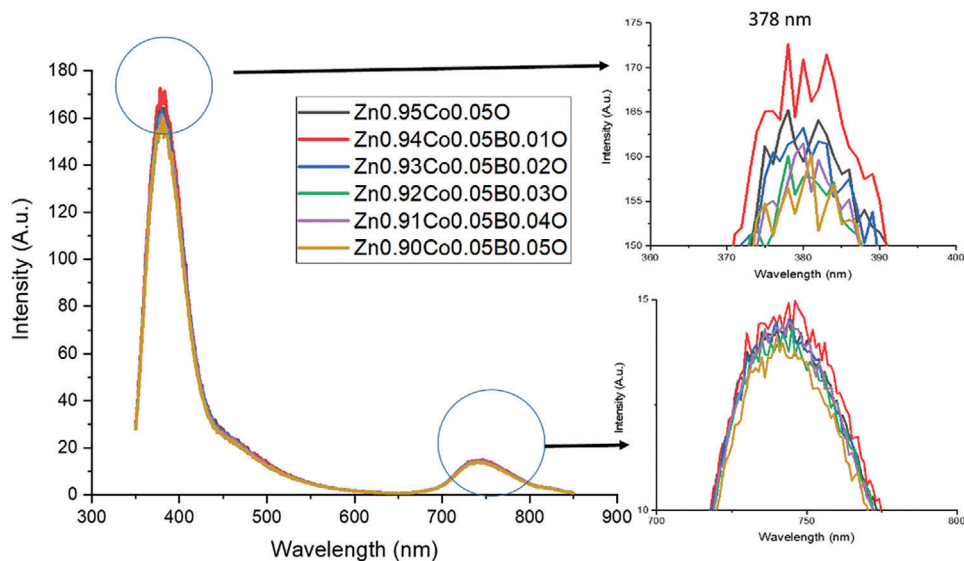
2.5. Optical Studies

2.5.1. UV–Vis Diffuse Reflectance Spectra

Figure 12 presents the reflectance spectra of $Zn_{0.95-x}B_xCo_{0.05}O$ NPs (with x values of 0.00, 0.01, 0.02, 0.03, 0.04, and 0.05). These spectra were generated using UV–vis diffuse reflectance spectra (DRS) measurements in the wavelength range of 300–800 nm. Notably, a noticeable absorption edge is shown in all of the graphs in Figure 12 at a wavelength of ≈365 nm, which is quite similar to the band gap of zinc oxide.

2.5.2. Band Gap Calculation

The following formula, which creates a relationship between the absorption coefficient (α) and the photon energy ($h\upsilon$), can be used to compute the optical band gap (E_g):

$$\alpha h\upsilon = k\left(h\upsilon - E_g\right)^{1/n} \tag{5}$$

**ADVANCED
SCIENCE NEWS**

www.advancedsciencenews.com

Particle
& Particle Systems Characterization

www.particle-journal.com

Figure 10. PL spectra varying with the concentration of sol–gel-prepared $Zn_{0.95-x}B_xCo_{0.05}O$ (x = 0.00, 0.01, 0.02, 0.03, 0.04, 0.05) NPs. Ultraviolet emission peak and a broad visible emission band zoomed figures are displayed in the right column.

Equation (5) uses k as an energy-independent constant and E_g as the optical band gap. We fixed the value of n to 1/2 since ZnO exhibits directly allowed transitions and $F(R_\alpha)$ is directly proportional to α. Thus, we can rewrite Equation (6) as follows:

$$F\left(R_\alpha\right)h\upsilon = k\left(h\upsilon - E_g\right)^{1/2} \tag{6}$$

in other words, $(F(R_\alpha)h\upsilon)^2 = k^2(h\upsilon - E_g)$. A linear fit in the least-squares sense, $\gamma(h\upsilon) = A \times h\upsilon + B$, was used to estimate the slope of the graph of $(F(R_\alpha)h\upsilon)^2$ in 350 and 400 nm. We use the error formula in Equation (7) to achieve this. This can be represented more simply as $(F(R_\alpha)h\upsilon)^2 = k^2(h\upsilon - E_g)$. The equation $\gamma(h\upsilon) = A \times h\upsilon + B$ was fitted linearly in the least-squares
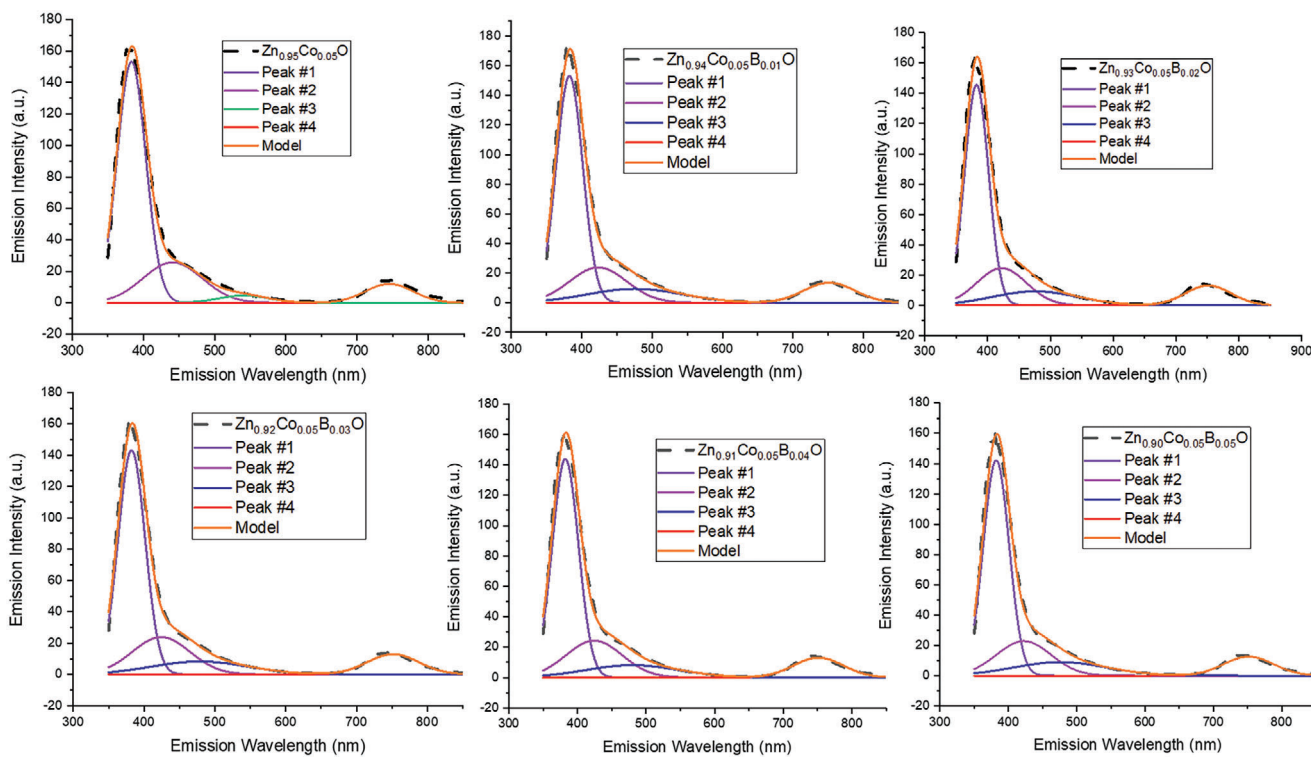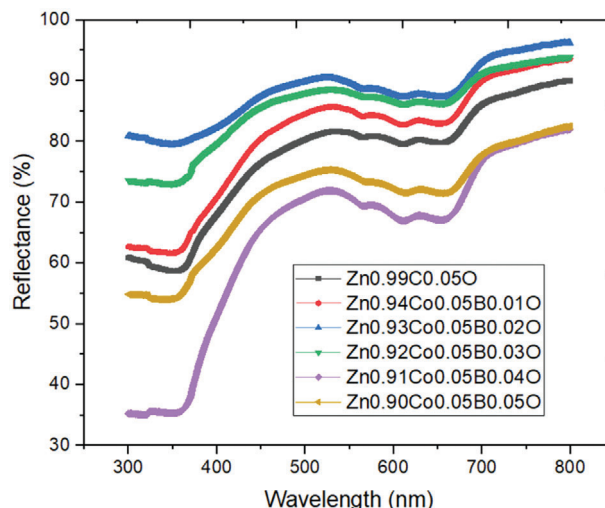

Figure 11. $Zn_{0.95-x}B_xCo_{0.05}O$ concentration dependence on emission intensity (a.u.) versus emission wavelength spectrum (x = 0.00, 0.01, 0.02, 0.03, 0.04, 0.05) NPs made using the sol–gel technique.

Table 3. The peak labels, center positions, and heights for different B concentrations of ZnCoBO NPs.

Peak Label	B [0%] Center	Height	B [1%] Center	Height	B [2%] Center	Height	B [3%] Center	Height	B [4%] Center	Height	B [5%] Center	Height	Emission Range	Emission Origin	NBE/DL Emission
Peak 1	380.28	153.19	379.46	153.1	379.36	145.59	379.379	143.145	379.4	143.79	379.168	142.25	UV	Exciton	NBE Emission
Peak 2	441.06	25.64	423.21	23.83	422.17	24.487	424.037	23.8508	424.4	24.27	422.469	22.84	Violet	$(Zn_i) \rightarrow (V_B)$	DL Emission
Peak 3			475.615	9.388	475.74	9.20	478.7	8.25	480.2	8.10	475.71	8.97	Blue	(V_{Zn})	
	541.04	4.59											Green	(V_O^+)	
Peak 4	745.04	11.98											Red	(V_O)	
			751.611	13.581	751.459	13.0908	751.432	12.9269	751.252	13.0698	751.64	12.5936	NIR (near-infrared)	(V_O)	

Figure 12. The reflectance spectra of $Zn_{0.95-x}B_xCo_{0.05}O$ NPs at various concentrations of B (Boron) are displayed.

method to determine the slope of the graph for $(F(R_\alpha)\, h\upsilon)^2$ within the 350–400 nm wavelength range. The following error formula, found in Equation (7), was applied to achieve this.

$$E\,(A, B) = \min_{A,\,B} \sum_{i=1}^{N} \left[A \times (h\upsilon)_i + B - \left(\left(F\left(R_\alpha\right) h\upsilon \right)^2 \right)_i \right]^2 \quad (7)$$

N is the total number of data points, and the minimizing technique was used to determine the ideal values of A and B. For this dataset, **Table 4** presents the values of A and B along with the band gap energies (E_g) and the corresponding relative error values.

As shown in Table 4 and **Figure 13a–f**, the band gap energies, E_g, were calculated by estimating the slope of the graph of $(F(R_\alpha)\, h\upsilon)^2$ to the photon energy axis, where $F\,(R_\alpha) = 0$. To put it another way, E_g was determined as $E_g = h\upsilon = -\frac{B}{A}$, which, as shown in Figure 13a–f represents the intersection point of the linear fit with the photon energy axis.

Based on these findings, the band gap energies of the B-doped ZnCoO NPs were determined to be within three decimal places, i.e., 2.980 to 3.174 eV. These changes in E_g values were caused by several factors, including crystallite size, carrier concentration, lattice strain, and the side effect of the dopant metals in the ZnO lattice.[3]

Table 4. Band gap energies (in eV) and relative errors were calculated for the $Zn_{0.95-x}B_xCo_{0.05}O$ NPs (with x values of 0.00, 0.01, 0.02, 0.03, 0.04, and 0.05) at different B doping ratios using the curve function $\gamma\,(h\upsilon) = A \times h\upsilon + B$.

Sample name	A	B	E_g [eV]	Rel. Error
$Zn_{0.95}Co_{0.05}O$	0.895	−2.816	3.174	3.75×10^{-5}
$Zn_{0.94}B_{0.01}Co_{0.05}O$	0.644	−2.054	3.152	2.148×10^{-5}
$Zn_{0.93}B_{0.02}Co_{0.05}O$	0.014	−0.040	2.98	2.16×10^{-7}
$Zn_{0.92}B_{0.03}Co_{0.05}O$	0.064	−0.193	3.087	4.54×10^{-7}
$Zn_{0.91}B_{0.04}Co_{0.05}O$	12.317	−38.291	3.080	4.65×10^{-3}
$Zn_{0.90}B_{0.05}Co_{0.05}O$	1.186	−3.677	3.069	1.083×10^{-4}
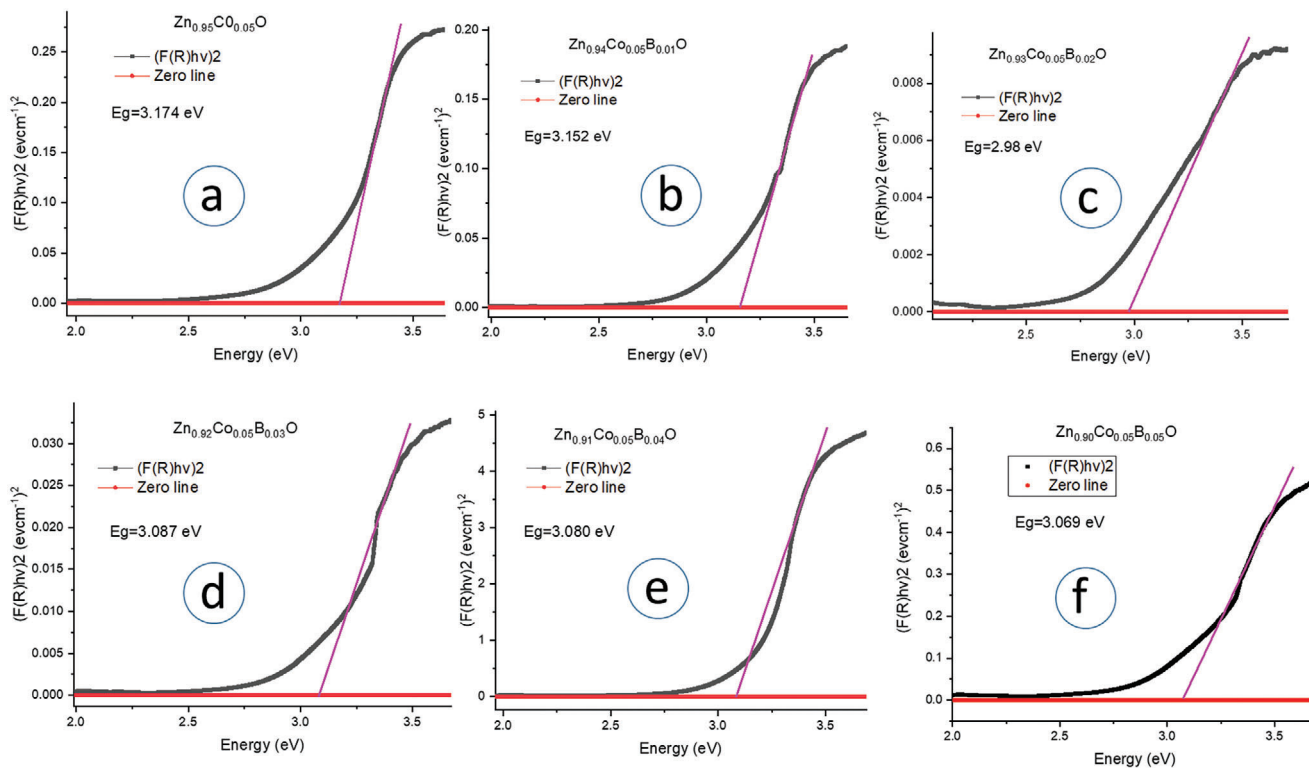
Figure 13. The linear fit and the plots of $(F(R_\alpha)h\nu)^2$ as a function of photon energy ($h\nu$) for a) $Zn_{0.95}Co_{0.05}O$, b) $Zn_{0.94}B_{0.01}Co_{0.05}O$, c) $Zn_{0.93}B_{0.02}Co_{0.05}O$, d) $Zn_{0.92}B_{0.03}Co_{0.05}O$, e) $Zn_{0.941}B_{0.04}Co_{0.05}O$, and f) $Zn_{0.90}B_{0.05}Co_{0.05}O$ NPs.

It was observed that the band gap of B-doped ZnCoO NPs varied depending on the crystallite size. Except for the 2% B doping, both the crystallite size and the band gap decreased with the addition of B doping to ZnCoO NPs as shown in **Figure 14b**. In nanomaterials, due to the quantum size effect where the size of particles can affect the band structure, larger particles typically have wider band gaps, while the band gap of particles at the nanometer scale can either widen or narrow. In our study, it was observed to be narrow.

The band gap is associated with the dislocation density (δ) and microstrain (ε) of the NPs. High dislocation density and microstrain can lead to irregularities in the crystal structure and disturbances in the arrangement of atoms. Due to the smaller ionic radius of B compared to Zn and Co, as observed in Figure 14c,d, the addition of B dopant (except for 2% B) increases the dislocation density (δ) and micros-

train (ε). This situation decreases the band structure and consequently reduces the band gap. Microstrain causes disruptions in the arrangement of atoms with the addition of B dopant.

2.5.3. Refractive Index Calculation

The major objectives of current studies are to achieve a high refractive index (n) and a broadband gap (E_g) because of their significant applications in the optoelectronics and sensor industries. The matching calculated values are shown in **Table 5**. The differences in refractive indices for the five models that resulted from changing the B content are displayed in **Figure 15**. The materials explored in this work (defined by $n > 2$ and $E_g > 3$) belong to the class of Transition Metals (TMs) possessing an empty d

Table 5. B concentration was taken into consideration when calculating the refractive indices using a variety of techniques. The results were presented precisely in two decimal places.

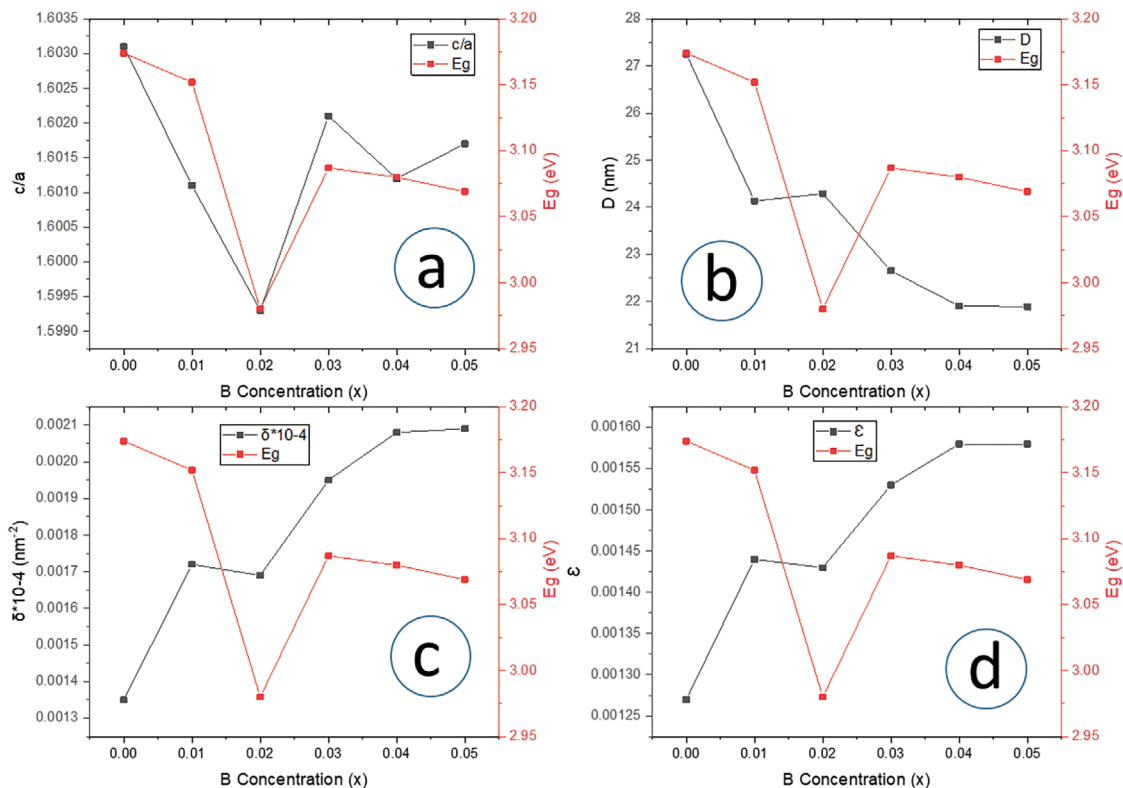| B concentration	E_g [eV]	Moss	Hervé and Vandamme	Kumar and Singh	Reddy and Anjayenulu	Ravindra et al.
0.00	3.17	2.34	2.28	2.32	2.72	2.12
0.01	3.15	2.34	2.28	2.33	2.73	2.13
0.02	2.98	2.38	2.33	2.37	2.77	2.24
0.03	3.09	2.36	2.30	2.34	2.74	2.17
0.04	3.08	2.36	2.31	2.34	2.74	2.17
0.05	3.07	2.36	2.31	2.35	2.75	2.18

Figure 14. Concentration-dependent band gap (E_g) and a) atomic packing factor (c/a), b) average crystallite size (D), c) dislocation density (δ), and d) microstrain (ε) values in $Zn_{0.95-x}B_xCo_{0.05}O$ structures (x = 0.00, 0.01, 0.02, 0.03, 0.04, and 0.05).
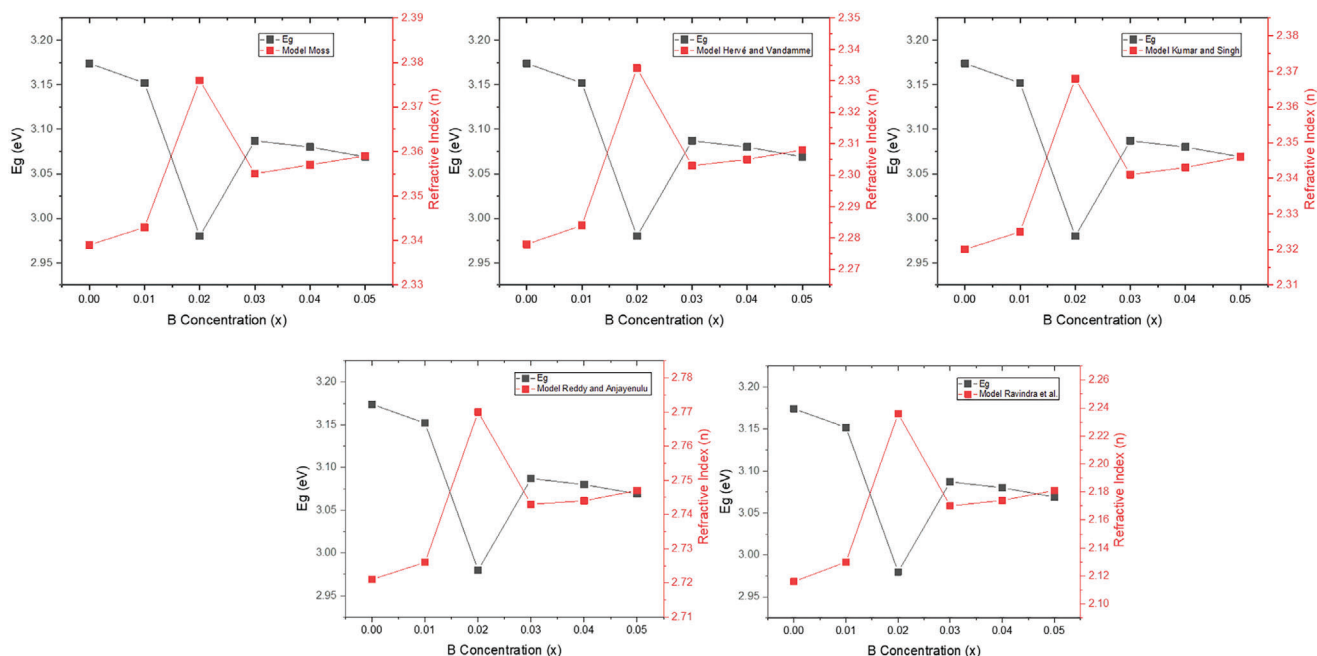

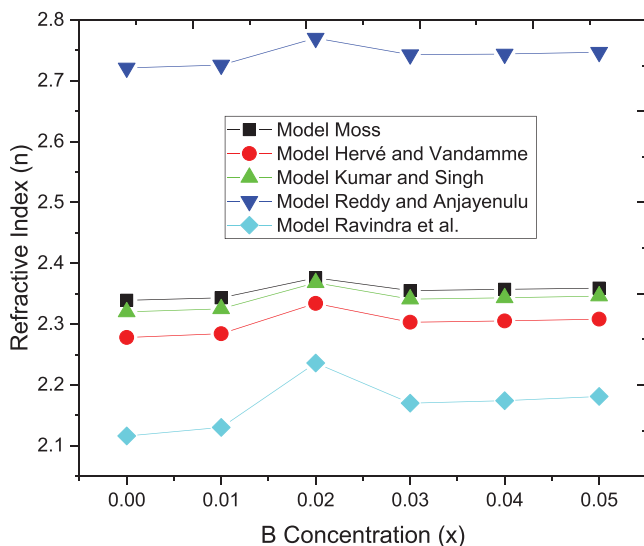**Figure 15.** $Zn_{0.95-x}B_xCo_{0.05}O$ structures: energy band gap as a function of B concentration (x) utilizing all five models.

**ADVANCED
SCIENCE NEWS**

www.advancedsciencenews.com

Particle

& Particle Systems Characterization

www.particle-journal.com

Figure 16. $Zn_{0.95-x}B_xCo_{0.05}O$ structures: refractive index as a function of B concentration (x).

shell which is consistent with the findings of Naccarato et al.,[9] as shown in Figure 15.

The following five models were used to calculate the refractive index:

Ravindra et al.[10] $n = 4.084 - 0.62 E_g$,

Moss[11] $n = \left(\frac{95}{E_g}\right)^{\frac{1}{4}}$,

Hervé and Vandamme[12] $n = \sqrt{1 + \left(\frac{13.6}{E_g + 3.47}\right)^2}$,

Reddy and Anjayenulu[13] $n = \left(\frac{154}{E_g - 0.365}\right)^{\frac{1}{4}}$, and finally.

The relationship $n = 3.3668 (E_g)^{-0.32234}$ was provided by Kumar and Singh,[14] and Table 5 records the computed data. It is important to note that all of the aforementioned models aside from the Ravindra model show an inverse relationship between band gap energy and refractive index, which is represented as $n \approx \left(\frac{1}{E_g}\right)^k$, $0.25 < k < 1$.

Figure 16 makes it clear that there is a constant pattern between the refractive index and energy band gap in all five models. Between 2.32 and 2.38, Moss[11] and Kumar and Singh[14] obtained comparable findings using these models. Based on these five models, Tripathy[47] offered dependability ranges for the energy band gaps, which were recorded in **Table 6**.

Table 6. Reliability ranges for the energy band gaps based on the models.

Model	Reliability ranges of band gaps
Ravindra et al.	1.50 eV < E_g < 3.50 eV
Moss	0.17 eV < E_g < 3.68 eV
Hervé and Vandamme	2.00 eV < E_g < 4.00 eV
Reddy and Anjayenulu	1.10 eV < E_g < 6.20 eV
Kumar and Singh	2.00 eV < E_g < 4.00 eV

Our computed energy band gap values, as shown in Table 5, were within the 2.980 eV to 3.174 eV range, which means that the refractive index values derived from these models are accurate. Notably, Table 5 shows that the approach suggested by Ravindra et al.[10] produced outcomes that resembled those reported by Chithra and Pushpanathan.[48]

3. Conclusion

Sol–gel was used to generate $Zn_{0.95-x}B_xCo_{0.05}O$ (x = 0.00, 0.01, 0.02, 0.03, 0.04, and 0.05) NPs. The structural and optoelectronic characteristics were examined based on the concentration levels of each component. An individual ZnO phase with a wurtzite hexagonal structure was revealed by X-ray diffraction investigation.

In B-doped ZnCoO NPs, due to the quantum size effect, it was found that the crystallite size and band gap of the NPs decreased as the B doping increased (except for 2% B doping). The change in band gap in B-doped ZnCoO NPs was associated with an increase in dislocation density (δ) and microstrain (Ɛ), leading to irregularities in the crystal structure and disruptions in the arrangement of atoms (except for 2% B doping). This situation decreased the band structure and consequently reduced the band gap.

The PL measurements displayed violet, blue, green, and red emissions. With boron (B) doping, a shift from green emission to blue emission is observed, indicating a transformation of singly charged oxygen vacancies (V_O^+) to V_{Zn} vacancies. Thus, acceptor defects can be utilized in desired sensor and optoelectronic applications. In optoelectronic applications, the relationship between band gap and refractive index is crucial. ZnCoO NPs exhibit the widest band gap, leading to lower conductivity and absorption of higher energy photons. With the addition of B doping, the band gap decreases, potentially leading to the absorption of lower energy photons. As the band gap decreases in B-doped ZnCoO NPs, the refractive index generally decreases as well (except for 2% B doping). This is because a lower band gap affects the electronic structure of NPs, allowing for the absorption of lower energy photons. However, it was observed from the obtained results that despite the decrease in the band gap, B-doped ZnCoO NPs could still be utilized in optoelectronic applications due to having a band gap above 3 eV and a refractive index above 2.

4. Experimental Section

Preparation of $Zn_{0.95-x}B_xCo_{0.05}O$ NPs: These NPs were synthesized by sol–gel method at various concentrations in the range ($Zn_{0.95-x}B_xCo_{0.05}O$) where x = 0.00 to 0.05 by highly pure chemicals (>99% purity) Zinc acetate dehydrate ($Zn(CH_3CO_2)22H_2O$), cobalt(II) acetate tetrahydrate ($Co(CH_3CO_2)24H_2O$), boric acid (H_3BO_3), 1 mL of Monoethanolamine, and 80 mL of Methanol. The synthesized NPs were annealed first at 450 °C for 10 min, which is expected to cool in the furnace for ≈3 h, and then kept at 600 °C for 30 min and after it cooled for ≈6 h.[3]

Characterization Techniques: Using CuKα radiation (λ = 1.5406 Å), the synthesized powders were subjected to phase analysis using a Rigaku Multiflex diffractometer. The 2θ range of 20°–80° was scanned, with increments of 0.02 and a scanning speed of 3° min⁻¹. Transmission Electron Microscope (TEM) and elemental analysis employing X-ray energy distribution (EDAX) were used to evaluate the surface morphologies of the resultant samples. With the use of a Shimadzu 2600 UV-Spectrophotometer,

measurements were made in the 200–900 nm range to evaluate the optical characteristics of the NPs. The Perkin Elmer Spectrum Two FTIR-ATR spectrophotometer was used to record the Fourier Transform Infrared (FTIR) spectra (4000–400 cm^{-1}). The Agilent Cary Eclipse Fluorescence Spectrophotometer was also used to assess the photoluminescence qualities.

Conflict of Interest

The authors declare no conflict of interest.

Data Availability Statement

The data that support the findings of this study are available from the corresponding author upon reasonable request.

[1] S. Y. Yurish, *Advances in Microelectronics: Reviews*, IFSA Publishing, Barcelona **2018**, Vol. *1*.

[2] I. Ahmad I, M. S. Akhtar, E. Ahmed, M. Ahmad, *J. Mater. Sci. Mater. Electron* **2020**, *31*, 1084.

[3] S. D. Senol, E. Ozugurlu, L. Arda, *Ceram. Int.* **2020**, *46*, 1084.

[4] H. Pan, Y. Zhang, Y. Hu, H. Xie, *Optik* **2020**, *208*, 164560.

[5] A. A. Azab, S. A. Esmail, M. K. Abdelamksoud, *Silicon* **2019**, *11*, 165.

[6] S. D. Senol, O. Ozturk, C. Terzioğlu, *Ceram. Int.* **2015**, *41*, 11194.

[7] Y. Gui, Y. Zhu, K. Tian, J. Wu, H. Guo, X. Qin, X. Qin, D. Guo, C. Fang, *Materials Science and Engineering* **2024**, *303*, 117328.

[8] A. Tun Naziba, M. Tun Nafisa, R. Sultana, M.d. Fahim Ehsan, A. R. M. Tareq, R. Rashid, H. Das, A. K. M. Atique Ullah, A. K. M. Fazle Kibria, *J. Magn. Magn. Mater.* **2024**, *593*, 171836.

[9] F. Naccarato, F. Ricci, J. Suntivich, G. Hautier, L. Wirtz, G.-M. Rignanese, *Phys. Rev. Materials* **2019**, *3*, 044602.

[10] N. M. Ravindra, S. Auluck, V. K. Srivastava, *Physica Status Solidi.* **1979**, *93*, K155.

[11] T. S. Moss, *Phys. Status Solidi B* **1985**, *131*, 415.

[12] P. Hervé, L. Vandamme, *Infrared Phys. Technol.* **1994**, *35*, 609.

[13] R. R. Reddy, S. Anjaneyulu, *Phys. Status Solidi B* **1992**, *174*, K91.

[14] V. Kumar, J. Singh, *Indian J. Pure Appl. Phys.* **2010**, *48*, 571.

[15] S. Noda, M. Fujita, T. Asano, *Nat. Photonics* **2007**, *1*, 449.

[16] S. P. Hoffmann, M. Albert, N. Weber, D. Sievers, J. Förstner, T. Zentgraf, C. Meier, *ACS Photonics* **2018**, *5*, 1933.

[17] C. Ronning, P. X. Gao, Y. Ding, Z. L. Wang, D. Schwen, *Appl. Phys. Lett.* **2004**, *84*, 783.

[18] Y.-W. Ra, K.-S. Choi, J.-H. Kim, Y.-B. Hahn, Y.-H. Im, *Small* **2008**, *4*, 1105.

[19] Y. Choi, J. Kang, D. Hwang, S. Park, *IEEE Trans. Electron Devices* **2010**, *57*, 26.

[20] J. B. Webb, D. F. Williams, M. Buchanan, *Appl. Phys. Lett.* **1981**, *39*, 640.

[21] Z. K. Tang, G. K. L. Wong, P. Yu, M. Kawasaki, A. Ohtomo, H. Koinuma, Y. Segawa, *Appl. Phys. Lett.* **1998**, *25*, 3270.

[22] D. R. Clarke, *J. Am. Ceram. Soc.* **1999**, *82*, 485.

[23] M. F. M. Noh, N. A. Arzaee, J. Safaei, N. A. Mohamed, H. P. Kim, A. R. M. Yusoff, J. Jang, M. A. M. Teridi, *J. Alloy. Comp.* **2019**, *773*, 997.

[24] E. Asikuzun, O. Ozturk, L. Arda, C. Terzioglu, *J. Mol. Struct.* **2018**, *1165*, 1.

[25] A. Guler, L. Arda, N. Dogan, C. Boyraz, E. Ozugurlu, *Ceram. Int.* **2019**, *45*, 1737.

[26] C. Boyraz, N. Dogan, L. Arda, *Ceram. Int.* **2017**, *43*, 15986.

[27] M. Tosun, L. Arda, *Ceram. Int.* **2019**, *45*, 16234.

[28] I. P. Duru, E. Ozugurlu, L. Arda, *Ceram. Int.* **2019**, *45*, 5259.

[29] S. D. Senol, C. Boyraz, E. Ozugurlu, A. Gungor, L. Arda, *Cryst. Res. Technol.* **2019**, *54*, 1800233.

[30] D. Akcan, S. Ozharar, E. Ozugurlu, L. Arda, *J. Alloy. Comp.* **2019**, *797*, 253.

[31] N. Doğan, A. Bingölbali, L. Arda, *J. Magn. Magn. Mater.* **2015**, *373*, 226.

[32] E. Asikuzun, O. Ozturk, L. Arda, C. Terzioglu, *J. Mater. Sci. Mater. Electron.* **2017**, *28*, 14314.

[33] L. Arda, *J. Magn. Magn. Mater.* **2019**, *475*, 493.

[34] U. Ozgur, Y. I. Alivov, C. Liu, A. Teke, M. A. Reshchikov, S. Dogan, V. Avrutin, S. J. Cho, H. Morkoc, *J. Appl. Phys* **2005**, *98*, 041301.

[35] Z. K. Heiba, L. Arda, M. B. Mohamed, N. Y. Mostafa, M. A. Al-Jalali, N. Dogan, *Nov. Magnetism* **2013**, *26*, 3299.

[36] T. Pandiyarajan, R. Udayabhaskar, B. Karthikeyan, *Appl. Phys. A* **2012**, *107*, 411.

[37] R. Siddheswaran, R. V. Mangalaraja, R. E. Avila, D. Manikandan, C. E. Jeyanthi, S. Ananthakumar, *Mater. Sci. Eng. A* **2012**, *558*, 456.

[38] M.d M. Ali, M. H. Kabir, *Optical Materials* **2024**, *148*, 114949.

[39] C. K. Macit, E. Gurgenc, F. Biryan, F. Özen, T. Gurgenc, C. Ozel, *J. Mater. Sci.: Mater. Electron.* **2023**, *34*, 2076.

[40] R. D. Shannon, C. T. Prewitt, *J. Inorg. Nucl. Chem.* **1970**, *32*, 1427.

[41] M. Ashokkumar, S. Muthukumaran, *J. Mater. Sci.* **2015**, *26*, 1225e1233.

[42] O. O. Akinwunmi, O. A. Akinwumi, J. A. O. Ogundeji, A. T. Famojuro, *Materials Sciences and Applications* **2018**, *09*, 844.

[43] K. Senturk, B. Yalcin, I. E. Yalcin, et al., *J. Mater. Sci.: Mater. Electron.* **2023**, *34*, 847.

[44] L. Arda, O. Karatas, M. C. Alphan, E. Ozugurlu, *Electron spin resonance and photoluminescence studies of Co/Mg co-doped ZnO nanoparticles* **2024**, *21*, 2458.

[45] S. D. Senol, E. Ozugurlu, L. Arda, *J. Alloys Compd.* **2020**, *822*, 153514.

[46] S. C. Singh, R. Gopal, *Appl. Surf. Sci.* **2012**, *258*, 2211.

[47] S. Tripathy, *Opt. Mater.* **2015**, *46*, 240.

[48] M. J. Chithra, K. Pushpanathan, *Mod. Phys. Lett. B* **2016**, *30*, 1650406.